ChemPhysChem

Research Article
doi.org/10.1002/cphc.202300303

Chemistry Europe
European Chemical
Societies Publishing

www.chemphyschem.org

Raman Spectroscopy of Formamidinium-Based Lead Mixed-Halide Perovskite Bulk Crystals

Supriya Ghosh+,[a, b] Debkumar Rana+,[a, c] Bapi Pradhan,[d] Patrice Donfack,[a] Johan Hofkens,[d, e] and Arnulf Materny*[a]

In recent years, there has been an impressively fast techno-logical progress in the development of highly efficient lead halide perovskite solar cells. Nonetheless, the stability of perovskite films and associated solar cells remains a source of uncertainty and necessitates sophisticated characterization techniques. Here, we report low- to mid-frequency resonant Raman spectra of formamidinium-based lead mixed-halide perovskites. The assignment of the different Raman lines in the measured spectra is assisted by DFT simulations of the Raman spectra of suitable periodic model systems. An important result of this work is that both experiment and theory point to an increase of the stability of the perovskite structure with increasing chloride doping concentration. In the Raman spectra, this is reflected by the appearance of new lines due to the formation of hydrogen bonds. Thus, higher chloride doping results in less torsional motion and lower asymmetric bending contributing to higher stability. This study yields a solid basis for the interpretation of the Raman spectra of formamidinium-based mixed-halide perovskites, furthering the understanding of the properties of these materials, which is essential for their full exploitation in solar cells.

Introduction

Lead halide perovskites (LHPs) have attracted considerable attention from researchers due to their outstanding optoelec-tronic properties such as a sharp absorption edge, high absorption coefficients, large diffusion length of free charge carriers, and low recombination rates.[1–5] During the last few years, LHPs have emerged as promising materials for light emitting diodes, solar cells, transistors, lasers, and memory devices.[6–10] A polycrystalline $MAPbI_3$-based p-i-n structural photovoltaic device shows power conversion efficiencies of more than 22%; the investigated device is (Poly[bis(4-phenyl)(2,4,6-trimethylphenyl)amine] : 2,3,5,6-Tetrafluoro7,7,8,8-tetracyanoquinodimethane (PTAA:F4TCNQ))/daminozide (DA)/perovskite:DA).[11] The high efficiency devices can be produced on cheap non-crystalline substrates by both vapor deposition and solution processing.[12,13] Despite the wide interest in LHPs, the characterization of their hybrid structures and the under-standing of their chemical-physical properties are still some-what elusive. The study of the structure and properties of these materials have been carried out by X-ray diffraction and UV-Vis spectroscopy, along with electronic structure calculations.[14–17]

Infrared and Raman spectroscopy have proven to be very useful for studying properties of hybrid perovskite materials.[18–21] Following reports of highly efficient solar cells fabricated with methyl ammonium lead iodide ($MAPbI_3$), many infrared absorption and Raman studies were performed.[22–24] For example, Raman spectroscopy can be used for in situ studies of devices fabricated on glass substrates, i.e., buried layers. Low-frequency lattice vibrations can also be detected by low wavenumber Raman spectroscopy.[25,26] It has been shown that due to the Fröhlich interaction, the scattering from longitudinal optical phonons dominates the electron scattering in metal halide double perovskites at room temperature, which results in multi-phonon processes up to the fourth order in the non-resonant Raman spectrum.[27] Furthermore, Raman spectro-scopy proved capable for the characterization of the surface structural changes that go hand in hand with perovskite decomposition upon light irradiation.[28]

Recently, high power-conversion efficiencies (PCEs) and improved material stability of perovskite devices have been achieved by using mixed composition perovskite materials obtained by partial substitution of A/X sites (in ABX_3 type perovskites) with alternative elements/molecules.[29,30] In the efficiency chart constantly updated by the National Renewable Energy Laboratory (NREL), nearly all efficiency records for

[a] Dr. S. Ghosh,+ Dr. D. Rana,+ Dr. P. Donfack, Prof. Dr. Dr. A. Materny
School of Science, Constructor University, Campus Ring 1, 28759 Bremen, Germany
E-mail: amaterny@constructor.university

[b] Dr. S. Ghosh+
Department of Chemistry and Biochemistry, The Ohio State University, 100 West 18th Avenue, Columbus, Ohio 43210, USA

[c] Dr. D. Rana+
Max-Born-Institut für Nichtlineare Optik und Kurzzeitspektroskopie, 12489 Berlin, Germany

[d] Dr. B. Pradhan, Prof. Dr. J. Hofkens
Department of Chemistry, KU Leuven, Celestijnenlaan 200F, 3001 Heverlee, Belgium

[e] Prof. Dr. J. Hofkens
Max Planck Institute for Polymer Research, Ackermannweg 10, 55128 Mainz, Germany

[+] These authors contributed equally

📰 Supporting information for this article is available on the WWW under https://doi.org/10.1002/cphc.202300303

perovskite solar cells have been achieved with such mixed A and/or X site hybrid perovskite structures.[31] Among possible compositions, (Formamidinium) FA-based perovskite materials have attracted significant attention due to a narrower more favorable band gap, an elevated decomposition temperature, and a more symmetric crystal structure compared to its MA counterpart.[4,20,32–35] At room temperature, FA-based perovskites such as $FAPbI_3$ undergo an $\alpha \rightarrow \delta$ phase transition, whereby the $(PbI_6)^{4-}$ octahedra are corner- and face-shared in α-$FAPbI_3$ and δ-$FAPbI_3$, respectively; for this reason, a mixture of cations and/ or halides are commonly used to stabilize the cubic perovskite structure.[28]

In this work, we have undertaken a Raman spectroscopic study on the more stable FA-based family. In particular, we have studied $FAPbBr_3$ systems with mixed halide compositions and carried out tentative Raman mode assignments. Our experimental study is also supported by density functional theory calculations. In the comparative analysis of the mixed-halide $FAPbBr_3$ systems, Raman spectral features are observed, which are correlated to the change of polarity, change of NH_2 torsional motion, and change of NH_2 asymmetric bending. Our results advance the understanding of FA-based perovskite materials, which is important for the realization of perovskite solar cells with improved efficiency and stability.

Methods

Spectroscopic Techniques

UV-Vis Absorption and Photoluminescence

For all optical measurements, the microcrystal particles from each sample were filled in 1 mm cuvettes. UV-Vis reflectance and photoluminescence (PL) spectra were taken using a Perkin Elmer Lambda 950 and an Edinburgh FLS980 spectrometer, respectively.

Raman Spectroscopy

A portable i-Raman Plus spectrometer (BWS465-785S, B&W Tek, USA) was used for Raman measurements. It features an easy-to-use fiber-coupled and compact Raman spectrometer with built-in parts including a detector, a near-infrared 785 nm laser source for excitation, and a fixed grating allowing a very wide spectral coverage up to 3350 cm^{-1} within a single detection window. In addition, the system is equipped with an optical fiber probe with an actual Raman cut-off at 47 cm^{-1} (better than the system specification). This allows low-wavenumber Stokes Raman shift detection as close as 65 cm^{-1} (the low Raman spectral range specification) or less from the laser line. The optical fiber probe head of the laser is optionally fitted into a narrow collimator lens tube in order to couple it with a compact microscope assembly, which enables detailed analysis through a microscope objective. This combination, including a x50 long working distance microscope objective with 0.50

numerical aperture, resulted in a beam spot size of ~30–35 μm on the sample. All spectra were recorded in a 180° back-scattering geometry. The spectral resolution of the system was approx. 4 cm^{-1}. The aromatic breathing mode of toluene at 1003.7 cm^{-1} was used for checking the wavenumber calibration of the system. The BWSpec Software (version 4.03_33, B&W Tek, USA) was used to control the i-Raman Plus spectrometer and to automatically monitor the laser power delivered to the sample.
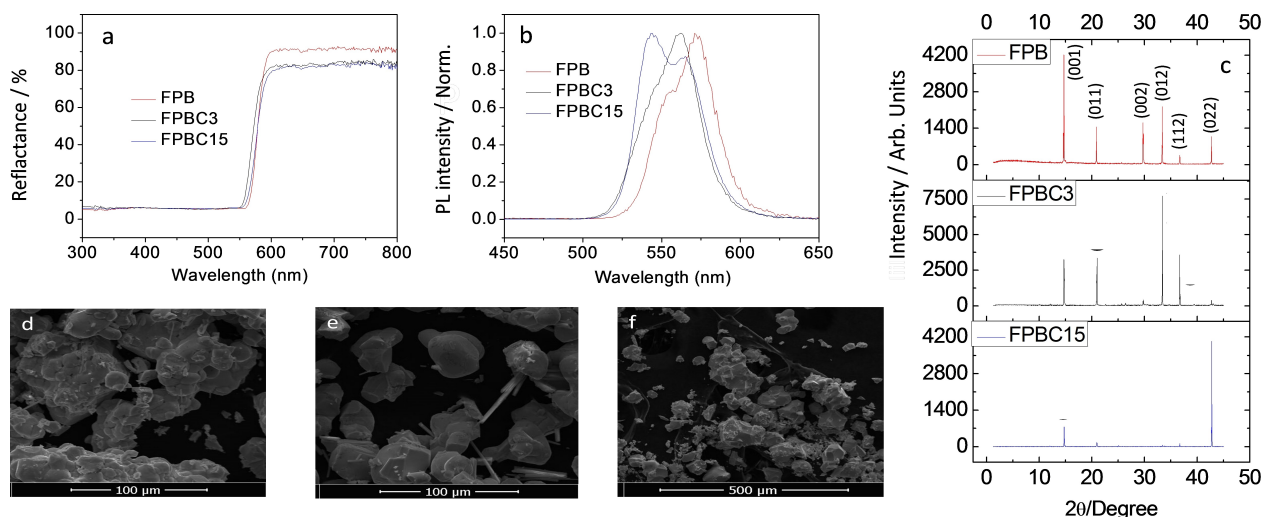
Computational Details

Density Functional Theory (DFT) calculations were carried out using Quantum Espresso,[36] an open-source computer code for electronic-structure calculations and materials modelling based on DFT, plane waves and pseudopotentials. We have used the generalized gradient approximation (GGA) in the Perdew-Burke-Ernzerhof version[37] for the exchange correlation potential. The plane-wave basis set was used to expand the electronic Kohn-Sham wave functions up to a kinetic energy cut-off of 70 Ry. As for k-points, we considered a 4×4×4 mesh of points distributed according to the Monkhorst-Pack algorithm within the first Brillouin zone of reciprocal lattice.[38]

Additionally, we have carried out more quantum mechanical calculations using the Gaussian 09 software package.[39] The ground-state structures of the separated cation FA^+ and $FABr_3$ have been optimized using the B3LYP and LSDA functionals with LanL2DZ basis set, respectively. For a better understanding of the effect of doping on the cation, we have optimized the ground-state structures of $FABr_2Cl$, $FABrCl_2$, and $FACl_3$ using the LSDA functional with LanL2DZ basis set. The same basis sets have been used to calculate the vibrational wavenumbers along with the Raman intensities. In each case, the optimized geometries converged to minima of the potential energy surfaces and no negative wave-numbers were found. GaussView 5 was used to analyze and visualize the data.[40]

Material Synthesis

$FAPbBr_{2.97}Cl_{0.03}$ (FPBC3): A mixture of 24 mg (0.3 mmol) of FACl (97%, Sigma), 587.4 mg (4.7 mmol) of FABr (98%, Sigma), 1.835 g (5 mmol) of $PbBr_2$ (98%, Sigma), 4 ml dimethylformamide (DMF), and 4 ml gamma-butyrolactone (GBL) was stirred overnight. The mixture was then filtered by a PTFE filter with 0.25 μm pore size and diluted with 4 ml DMF. Then 20 ml toluene was quickly added in the above stirred solution (400 rpm) at 80 °C for 10 min. Immediately after the addition of toluene, orange color precipitates formed, indicating the formation of perovskite microcrystals.[41] Finally, the microcrystals were centrifuged twice for 5 minutes at 3000 rpm, the entire supernatant was carefully decanted, and the precipitates were dried in vacuo at 60 °C for 12 hours to obtain a powder of microcrystals.

$FAPbBr_{2.85}Cl_{0.15}$ (FPBC15) and $FAPbBr_3$ (FPB) microcrystals were synthesized similarly like the above mentioned protocol using stoichiometric molar salt ratios. For example, 60 mg of 0.75 mmol FACl, 531.1 mg of 4.25 mmol FABr, 1.835 g of 5 mmol $PbBr_2$ for FPBC15 and 1.835 g of 5 mmol $PbBr_2$ and 0.625 g of 5 mmol FABr for FPB were used.

ChemPhysChem

Research Article
doi.org/10.1002/cphc.202300303

Chemistry Europe
European Chemical
Societies Publishing

Figure 1. (a) UV-Vis reflection and (b) emission spectra of FPB (red), FPBC3 (black), FPBC15 (blue). (c) X-ray diffraction patterns of FPB (red), FPBC3 (black), FPBC15 (blue) with assignments of lines. (d)–(f) Scanning electron microscopy images of FPB, FPBC3, and FPBC15.

Results and Discussion

Figure 1 shows the reflection and emission spectra of FPB, FPBC3, and FPBC15. Panel (a) shows that the edge of FPBC15 reflectance spectrum shifts towards shorter wavelengths with increasing Cl-doping concentration, which indicates that the optical band gap of FAPC15 is shifted towards the higher energy side. Furthermore, we observe in panel (b) that the PL spectra of FPBC3 and FPBC15 are blue shifted compared to FPB due to the doping with the chloride ion (Cl$^-$). This is in accordance to earlier findings by Li et al.[42] who observed that the incorporation of chloride ions into the CsPbBr$_3$ lattice results in a shift of the emission from green to blue. In our case, the largest blue shift is found for FPBC15 where the amount of Cl$^-$ doping is the highest. Furthermore, we observed multiple emission peaks in all three perovskites. This can be attributed to the presence of multiple phases as bulk perovskites undergo an $\alpha \rightarrow \delta$ phase transition, where α represents the cubic and δ the tetragonal structure.[43,44] Cubic perovskite structures are stabilized by using mixture with halides. Panel (c) of Figure 1 show the X-ray diffraction patterns and panels (d)-(f) show scanning electron microscopy images confirming the formation of nanometer-sized particles of FPB, FPBC3, and FPBC15.

Before analyzing the measured Raman spectra in detail, in the following, we briefly discuss the outcome of the theoretical simulation performed for the considered perovskite systems. In Figure 2, we present the optimized structures of (a) FAPbBr$_3$ and FAPbBr$_3$ doped with (b) 1, (b) 2, and (d) 3 Cl$^-$ ions.

In our calculation, it is difficult to mimic the same doping concentration used in experiment (FPBC3 and FPBC15; see above). If we would like to maintain the similar doping concentration used in our experiment for FPBC15, the optimized structure should contain 8787 atoms, shown in Figure S1. The optimization of such a system with a huge number of atoms would be difficult using our computer facilities. Therefore, we have optimized each structure with a smaller unit,
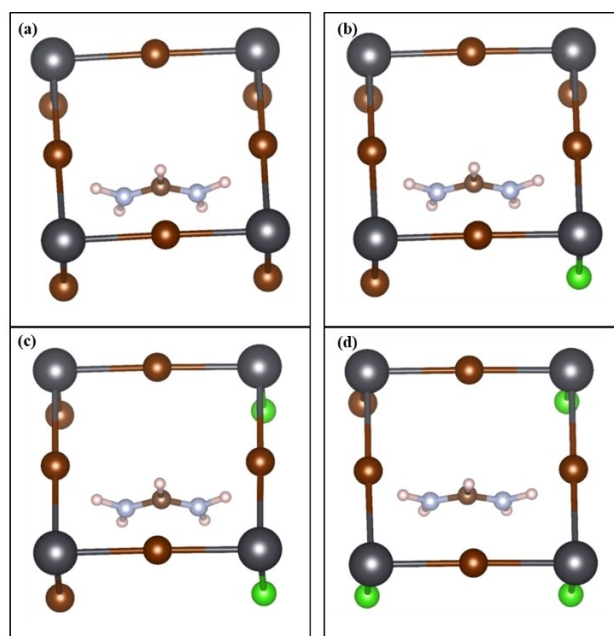
Figure 2. Optimized structures of (a) undoped FAPbBr$_3$, FAPbBr$_3$ with (b) 1 Cl$^-$, (c) 2 Cl$^-$, and (d) 3 Cl$^-$ ions added.

which contains 20 atoms including 1 C, 2 N, 5 H, 4 Pb, and 7 Br atoms. For the doped structures, we have replaced the Br atoms by Cl atoms. The simulation with 20 atoms has proven to give reasonable results reflecting the changes of the overall system, as we try to observe the effect of doping on the relaxation energy. The parameters for the different structural models optimized are given in Table 1. The DFT calculated lattice constants are very close to the lattice constants calculated based on the XRD spectra (Table S8). Theoretical calculations are performed by considering the cubic structure of the perovskite. Due to the good consistency of DFT calculations and XRD results, we consider the perovskite structure at room temperature to be dominated by the cubic phase. This is also in

ChemPhysChem

Research Article
doi.org/10.1002/cphc.202300303

Chemistry
Europe
European Chemical
Societies Publishing

Table 1. Parameters of the optimized structures.

Structure	X (Å)	Y (Å)	Z (Å)
FAPbBr$_3$	6.516288636	0.000468145	−0.000000002
	0.000463832	6.891729190	−0.000000008
	−0.000000002	−0.000000008	6.432312404
FAPbBr$_3$ with 1 Cl	6.516288636	0.000468145	−0.000000002
	0.000463832	6.891729190	−0.000000008
	−0.000000002	−0.000000008	6.432312404
FAPbBr$_3$ with 2 Cl	6.523509662	0.000489153	−0.000029691
	0.000484510	6.890126203	−0.003588199
	−0.000029405	−0.003629573	6.432606188
FAPbBr$_3$ with 3 Cl	6.541632372	0.000520085	0.000018069
	0.000514550	6.886938144	−0.004141912
	0.000017815	−0.004189316	6.433790429

agreement with findings presented in previous publications.[43,44]

The relaxation and self-consistent field (SCF) energy for all the optimized structures are shown in Table 2.

We find that with the increment of Cl$^−$-doping concentration, the relaxation energy decreases. This indicates that the doping stabilizes the structure. Kooijman et al.[45] reported that doping LHPs with a few percent of zinc-halides improves their stability at ambient conditions and enhances the efficiency of the corresponding solar cell devices. Abdelhady et al.[46] reported an increase of the conductivity by four orders of magnitude and a significant bandgap narrowing due to hetero-valent doping of MAPbBr3 with Bi^{3+}. Snaith and coworkers[47] describe that a small amount of Al^{3+} doping results in better crystallization with fewer crystal defects in the film of MAPbBr3. However, the exact roles of those dopants are still not entirely clear.[45]

The optimized structures of different parts of the lead bromide-based perovskites are shown in Figure 3. The optimized ground state energies have been listed in Table 2.

For the simulation of the Raman spectral, we have focused on the isolated parts of the investigated structures. The vibrational modes obtained from the simulated Raman spectra are listed in Tables S1–S5. The analysis of the simulated Raman spectra provides a basis for the assignment of the Raman bands observed in the experiment to specific vibrational modes. From this assignment, further information about the influence of the doping concentration on the cations can be obtained.

Table 2. Relaxation and SCF energies of optimized FAPbBr$_3$ structures.

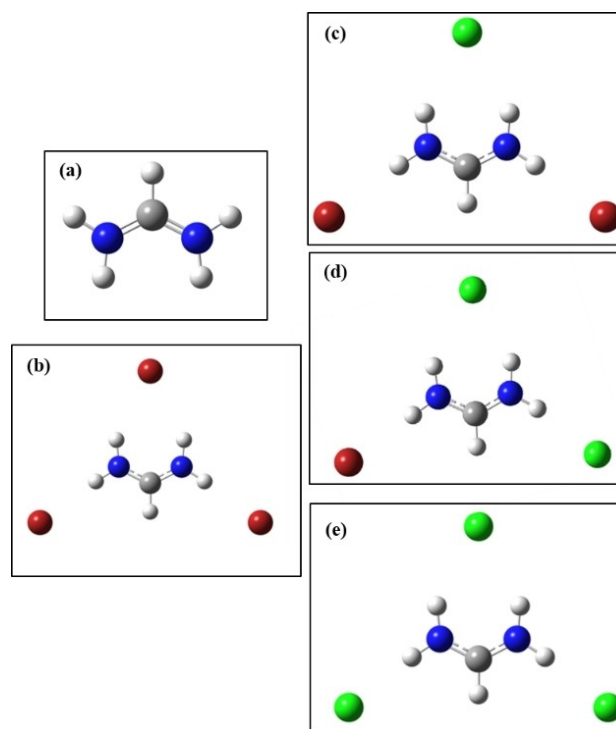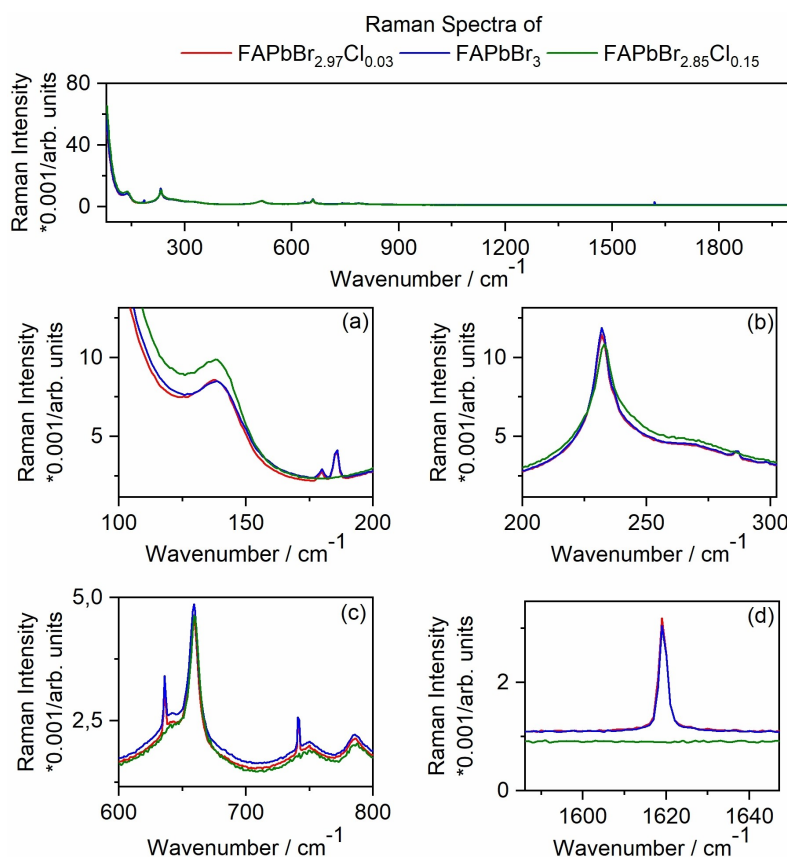| Structure	Relaxation energy (Ry)	SCF energy (Ry)
FAPbBr$_3$	−7091.80929955	−6742.02411488
FAPbBr$_3$, with 1 Cl	−6701.92428085	−6742.02411488
FAPbBr$_3$ with 2 Cl	−6352.60623323	−6372.69924590
FAPbBr$_3$ with 3 Cl	−5963.65199113	−6003.74749035

Figure 3. Optimized structures of different parts of the lead bromide-based perovskites: (a) FA$^+$, (b) FABr$_3$, (c) FABr$_2$Cl, (d) FABrCl$_2$, and (e) FABrCl$_3$.

For the experimental Raman measurements, we have used a laser at 785 nm to avoid laser-induced degradations. The Raman spectra were taken from FPB, FPBC3, and FPBC15 powder samples. The spectra are analogous to those reported earlier for perovskite samples. Figure 4 shows the Raman spectra obtained from the three samples. The Raman band at 141 cm^{-1} is in good agreement with results reported earlier.[19] It is due to the libration of cations involving the deformation of the inorganic cage. This Raman band is more intense for FPBC15 than for FPBC3 and FPB. A possible reason for the increased intensity is the higher molecular polarizability in FPBC15, as the Raman intensities are proportional to the square of the changes of the polarizabilities.[48] Our theoretical results show a higher dipole moment of FPBC15 compared to FPBC3 and FPB (Table S6), which might influence this mode.

The relation between polarizability and dipole moment can be expressed by equation (1):[48]

$$\alpha = - \int \widehat{\mu}^{eff} \delta\rho(r) \, dr \qquad (1)$$

where α is the molecular polarizability, $\widehat{\mu}^{eff}$ is the effective dipole operator, $\delta\rho(r)$ the linear change in the electron density of a molecule due to an external electric field and r is a vector in a space. The band observed at 230 cm^{-1} is mainly determined by the torsional motion of the FA cations. This is confirmed by the absence of this band in CPB. The band observed at ~500 cm^{-1} can be assigned to the NCN bending, the band at 625 cm^{-1} to the NH$_2$ torsion, and the band around 675 cm^{-1} to the NH$_2$ wagging mode. We note that the band at

ChemPhysChem

Research Article
doi.org/10.1002/cphc.202300303

**Chemistry
Europe**

European Chemical
Societies Publishing

Figure 4. Raman spectra of FPB (blue), FPBC3 (red), and FPBC15 (green). Panels (a), (b), (c), and (d) show different wavenumber regions of the spectrum for enhanced clarity.

$625\ cm^{-1}$ is absent for FPBC15. Insights into the NH_2 torsional mode suppression in FPBC15 can be gained from earlier studies. The band near $800\ cm^{-1}$ can be assigned to the CN stretching mode. Furthermore, we observe a Raman mode at $1620\ cm^{-1}$ for FPB and FPBC3, which is absent for FPBC15. This band can be assigned to asymmetric molecular bending.[49] The absences of this mode in the FPBC15 Raman spectrum indicate a higher structural stability of FPBC15 compared to FPBC3 and FPB.

We have performed a band-profile analysis using a standard spectral deconvolution with pseudo-Voigt functions given by equation (2) over the whole range as described earlier:[18]

$$y = y_0 + A\{\mu\left(\frac{2}{\pi}\right)\left(\frac{w}{4(x-xc)^2 + w^2}\right)$$
$$+(1-\mu)\sqrt{\frac{4\ln(2)}{w\sqrt{\pi}}}\exp\left[-\left(\frac{4\ln(2)(x-xc)^2}{w^2}\right)\right]\} \qquad (2)$$

where y_0 is an offset, A is amplitude, μ is the profile shape factor, w is the full width at half maximum (FWHM), and xc is the line position. With optimum fitting parameters in equation (2), we have obtained quasi-Lorentzian profiles for all bands. The fitted curves and the deconvolution components of the Raman spectra for FPB, FPBC3 and FPBC15 are shown in Figure 5. Among all the extracted parameters, we have focused

on the FWHM of different components, which are listed in Table S7 for the three different samples.

From the deconvolution analysis, we find that the FWHM values change significantly. For example, we find that the FWHM values of the $230\ cm^{-1}$ band (due to the torsional motion of the FA cations) are getting larger with increment of the doping concentration. This can also be observed for other corresponding Raman bands. In addition, band positions shift to higher wavenumbers. An increased FWHM of the torsional motion lines in doped perovskite indicates that torsional frequencies are spread over a large range of values. Previously, it has been described that the wider range of torsional frequencies is a result of hydrogen bonding and cation deformation.[19,50,51] Furthermore, the shift of the torsional mode towards higher wavenumber values indicates the structural change and relates to the stability of this perovskite materials.

Conclusions

The effect of Cl-doping of $FAPbBr_3$ was investigated experimentally and theoretically by using linear Raman spectroscopy and DFT simulations, respectively. The bandgap of the FAPbBr3 perovskites is increased (blue shift) with increasing chloride doping concentration due to a structural change. XRD analysis confirms the change of the crystal structure when the doping
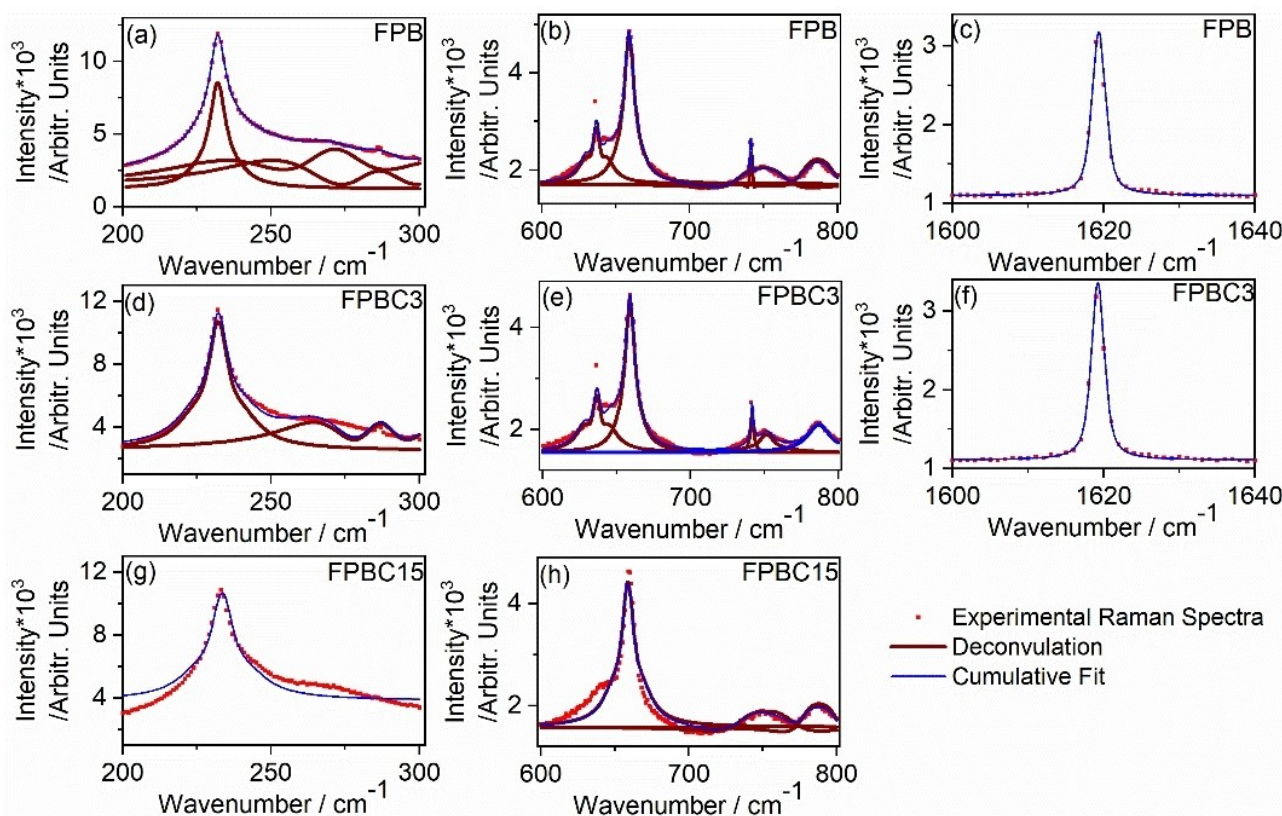
Figure 5. Fitted Raman bands of (a–c) FPB, (d–f) FPBC3 and (g, h) FPBC15 measured with 785 nm excitation. The red dotted curves are used for the experimental Raman spectra; the blue lines show the cumulative fitting results, and the deconvolution components are shown by brown lines.

concentration is increased. Our results from Raman spectroscopy and DFT calculation show that the higher Cl-doped structures (FAPbBr$_{2.85}$Cl$_{0.15}$ (FPBC15)) are more stable. The DFT calculations for isolated cations also yield a similar trend. The changes in the low-frequency modes and the absence of the NH$_2$ torsional and asymmetric molecular bending modes for the system with the highest concentration of Cl dopant point to a higher stability of the structure where the formation of hydrogen bonds plays an important role.

Acknowledgements

Conflict of Interests

The authors declare no conflict of interest.

Data Availability Statement

The data that support the findings of this study are available from the corresponding author upon reasonable request.

[1] Y. Chen, J. Yin, Q. Wei, C. Wang, X. Wang, H. Ren, S. F. Yu, O. M. Bakr, O. F. Mohammed, M. Li, *Nat. Photonics* **2022**, 1–6.
[2] C. Chen, T. Xuan, W. Bai, T. Zhou, F. Huang, A. Xie, L. Wang, R.-J. Xie, *Nano Energy* **2021**, *85*, 106033.
[3] S. Ghosh, B. Pradhan, Y. Zhang, M. B. J. Roeffaers, J. Hofkens, K. J. Karki, A. Materny, *J. Phys. Chem. C* **2022**, *126*, 478–486.
[4] S. Ghosh, Q. Shi, B. Pradhan, P. Kumar, Z. Wang, S. Acharya, S. K. Pal, T. Pullerits, K. J. Karki, *J. Phys. Chem. Lett.* **2018**, *9*, 4245–4250.
[5] Y. Hassan, J. H. Park, M. L. Crawford, A. Sadhanala, J. Lee, J. C. Sadighian, E. Mosconi, R. Shivanna, E. Radicchi, M. Jeong, *Nature* **2021**, *591*, 72–77.
[6] A. Kojima, K. Teshima, Y. Shirai, T. Miyasaka, *J. Am. Chem. Soc.* **2009**, *131*, 6050–6051.
[7] Y.-H. Kim, S. Kim, A. Kakekhani, J. Park, J. Park, Y.-H. Lee, H. Xu, S. Nagane, R. B. Wexler, D.-H. Kim, *Nat. Photonics* **2021**, *15*, 148–155.

ChemPhysChem

Research Article
doi.org/10.1002/cphc.202300303

Chemistry Europe
European Chemical
Societies Publishing

[8] A. P. Schlaus, M. S. Spencer, K. Miyata, F. Liu, X. Wang, I. Datta, M. Lipson, A. Pan, X.-Y. Zhu, *Nat. Commun.* **2019**, *10*, 1–8.

[9] W. Yu, F. Li, L. Yu, M. R. Niazi, Y. Zou, D. Corzo, A. Basu, C. Ma, S. Dey, M. L. Tietze, *Nat. Commun.* **2018**, *9*, 1–10.

[10] Y. Park, S. H. Kim, D. Lee, J.-S. Lee, *Nat. Commun.* **2021**, *12*, 3527.

[11] Y. Xu, S. Xiong, S. Jiang, J. Yang, D. Li, H. Wu, X. You, Y. Zhang, Z. Ma, J. Xu, J. Tang, Y. Yao, Z. Sun, Q. Bao, *Adv. Energy Mater.* **2023**, *13*, 2203505.

[12] M. Saliba, T. Matsui, K. Domanski, J.-Y. Seo, A. Ummadisingu, S. M. Zakeeruddin, J.-P. Correa-Baena, W. R. Tress, A. Abate, A. Hagfeldt, M. Grätzel, *Science* **2016**, *354*, 206–209.

[13] I. Hussain, H. P. Tran, J. Jaksik, J. Moore, N. Islam, M. J. Uddin, *Emergent Mater.* **2018**, *1*, 133–154.

[14] R. V. Vedrinskii, V. L. Kraizman, A. A. Novakovich, V. D. Ph, S. V. Urazhdin, *J. Phys. Condens. Matter* **1998**, *10*, 9561.

[15] S. Yun, X. Zhou, J. Even, A. Hagfeldt, *Angew. Chem. Int. Ed.* **2017**, *56*, 15806–15817.

[16] S. Ghosh, B. Pradhan, Y. Zhang, D. Rana, D. Naumenko, H. Amenitsch, J. Hofkens, A. Materny, *J. Phys. Chem. C* **2021**, *125*, 7799–7807.

[17] S. Ghosh, B. Pradhan, W. Lin, Y. Zhang, L. Leoncino, P. Chabera, K. Zheng, E. Solano, J. Hofkens, T. Pullerits, *J. Phys. Chem. Lett.* **2023**, *14*, 1066–1072.

[18] S. Ghosh, D. Rana, B. Pradhan, P. Donfack, J. Hofkens, A. Materny, *J. Raman Spectrosc.* **2021**, *52*, 2338–2347.

[19] C. Quarti, G. Grancini, E. Mosconi, P. Bruno, J. M. Ball, M. M. Lee, H. J. Snaith, A. Petrozza, F. De Angelis, *J. Phys. Chem. Lett.* **2014**, *5*, 279–284.

[20] S. Ruan, D. P. McMeekin, R. Fan, N. A. S. Webster, H. Ebendorff-Heidepriem, Y.-B. Cheng, J. Lu, Y. Ruan, C. R. McNeill, *J. Phys. Chem. C* **2020**, *124*, 2265–2272.

[21] M. Ledinský, P. Löper, B. Niesen, J. Holovský, S.-J. Moon, J.-H. Yum, S. De Wolf, A. Fejfar, C. Ballif, *J. Phys. Chem. Lett.* **2015**, *6*, 401–406.

[22] B.-w. Park, S. M. Jain, X. Zhang, A. Hagfeldt, G. Boschloo, T. Edvinsson, *ACS Nano* **2015**, *9*, 2088–2101.

[23] M. Badrooj, F. Jamali-Sheini, N. Torabi, *J. Phys. Chem. C* **2020**, *124*, 27136–27147.

[24] K. E. A. Hooper, H. K. H. Lee, M. J. Newman, S. Meroni, J. Baker, T. M. Watson, W. C. Tsoi, *Phys. Chem. Chem. Phys.* **2017**, *19*, 5246–5253.

[25] B. Zhang, J. Klarbring, F. Ji, S. I. Simak, I. A. Abrikosov, F. Gao, G. Y. Rudko, W. M. Chen, I. A. Buyanova, *J. Phys. Chem. C* **2023**, *127*, 1908–1916.

[26] Y. Yang, J. P. Robbins, L. Ezeonu, Y. Ma, N. Sparta, X. Kong, S. Strauf, S. G. Podkolzin, S. S. Lee, *J. Mater. Chem. C* **2020**, *8*, 8896–8903.

[27] J. A. Steele, P. Puech, M. Keshavarz, R. Yang, S. Banerjee, E. Debroye, C. W. Kim, H. Yuan, N. H. Heo, J. Vanacken, *ACS Nano* **2018**, *12*, 8081–8090.

[28] J. A. Steele, H. Yuan, C. Y. Tan, M. Keshavarz, C. Steuwe, M. B. Roeffaers, J. Hofkens, *ACS Nano* **2017**, *11*, 8072–8083.

[29] J. W. Xiao, L. Liu, D. Zhang, N. De Marco, J. W. Lee, O. Lin, Q. Chen, Y. Yang, *Adv. Energy Mater.* **2017**, *7*, 1700491.

[30] J. Hieulle, X. Wang, C. Stecker, D.-Y. Son, L. Qiu, R. Ohmann, L. K. Ono, A. Mugarza, Y. Yan, Y. Qi, *J. Am. Chem. Soc.* **2019**, *141*, 3515–3523.

[31] L. Kazmerski, *National Renewable Energy Laboratory (NREL)* 2012.

[32] V. C. Nair, C. Muthu, A. L. Rogach, R. Kohara, V. Biju, *Angew. Chem. Int. Ed.* **2017**, *56*, 1214–1218.

[33] S. Ghosh, Q. Shi, B. Pradhan, A. Mushtaq, S. Acharya, K. J. Karki, T. Pullerits, S. K. Pal, *J. Phys. Chem. Lett.* **2020**, *11*, 1239–1246.

[34] Y. Numata, N. Shibayama, T. Miyasaka, *J. Mater. Chem. A* **2022**, *10*, 672–681.

[35] J. Wang, J. Peng, Y. Sun, X. Liu, Y. Chen, Z. Liang, *Adv. Electron. Mater.* **2016**, *2*, 1600329.

[36] P. Giannozzi, S. Baroni, N. Bonini, M. Calandra, R. Car, C. Cavazzoni, D. Ceresoli, G. L. Chiarotti, M. Cococcioni, I. Dabo, A. Dal Corso, S. De Gironcoli, S. Fabris, G. Fratesi, R. Gebauer, U. Gerstmann, C. Gougoussis, A. Kokalj, M. Lazzeri, L. Martin-Samos, N. Marzari, F. Mauri, R. Mazzarello, S. Paolini, A. Pasquarello, L. Paulatto, C. Sbraccia, S. Scandolo, G. Sclauzero, A. P. Seitsonen, A. Smogunov, P. Umari, R. M. Wentzcovitch, *J. Phys. Condens. Matter* **2009**, *21*, 395502.

[37] J. P. Perdew, K. Burke, M. Ernzerhof, *Phys. Rev. Lett.* **1996**, *77*, 3865–3868.

[38] H. J. Monkhorst, J. D. Pack, *Phys. Rev. B* **1976**, *13*, 5188–5192.

[39] M. J. Frisch, G. W. Trucks, H. B. Schlegel, G. E. Scuseria, M. A. Robb, J. R. Cheeseman, G. Scalmani, V. Barone, B. Mennucci, G. A. Petersson, H. Nakatsuji, M. Caricato, X. Li, H. P. Hratchian, A. F. Izmaylov, J. Bloino, G. Zheng, J. L. Sonnenberg, M. Hada, M. Ehara, K. Toyota, R. Fukuda, J. Hasegawa, M. Ishida, T. Nakajima, Y. Honda, O. Kitao, H. Nakai, T. Vreven, J. A. Montgomery, Jr., J. E. Peralta, F. Ogliaro, M. Bearpark, J. J. Heyd, E. Brothers, K. N. Kudin, V. N. Staroverov, R. Kobayashi, J. Normand, K. Raghavachari, A. Rendell, J. C. Burant, S. S. Iyengar, J. Tomasi, M. Cossi, N. Rega, J. M. Millam, M. Klene, J. E. Knox, J. B. Cross, V. Bakken, C. Adamo, J. Jaramillo, R. Gomperts, R. E. Stratmann, O. Yazyev, A. J. Austin, R. Cammi, C. Pomelli, J. W. Ochterski, R. L. Martin, K. Morokuma, V. G. Zakrzewski, G. A. Voth, P. Salvador, J. J. Dannenberg, S. Dapprich, A. D. Daniels, Ö. Farkas, J. B. Foresman, J. V. Ortiz, J. Cioslowski, and D. J. Fox, *R. A. Gaussian09, Inc., Wallingford CT* 2009, *121*, 150–166.

[40] R. Dennington, T. Keith, J. Millam, *GaussView, 5.0.8; Gaussian Inc.* 2008.

[41] F. Zhang, B. Yang, K. Zheng, S. Yang, Y. Li, W. Deng, R. He, *Nano-Micro Lett.* **2018**, *10*, 1–8.

[42] Z. Li, Z. Chen, Y. Yang, Q. Xue, H.-L. Yip, Y. Cao, *Nat. Commun.* **2019**, *10*, 1027.

[43] T. Chen, B. J. Foley, C. Park, C. M. Brown, L. W. Harriger, J. Lee, J. Ruff, M. Yoon, J. J. Choi, S.-H. Lee, *Sci. Adv.* **2016**, *2*, e1601650.

[44] C. C. Stoumpos, C. D. Malliakas, M. G. Kanatzidis, *Inorg. Chem.* **2013**, *52*, 9019–9038.

[45] A. Kooijman, L. A. Muscarella, R. M. Williams, *Appl. Sci.* **2019**, *9*, 1678.

[46] A. L. Abdelhady, M. I. Saidaminov, B. Murali, V. Adinolfi, O. Voznyy, K. Katsiev, E. Alarousu, R. Comin, I. Dursun, L. Sinatra, *J. Phys. Chem. Lett.* **2016**, *7*, 295–301.

[47] P. K. Nayak, M. Sendner, B. Wenger, Z. Wang, K. Sharma, A. J. Ramadan, R. Lovrinčić, A. Pucci, P. Madhu, H. J. Snaith, *J. Am. Chem. Soc.* **2018**, *140*, 574–577.

[48] X. Chen, P. Liu, Z. Hu, L. Jensen, *Nat. Commun.* **2019**, *10*, 2567.

[49] F. H. Naqvi, J.-H. Ko, T. H. Kim, C. W. Ahn, Y. Hwang, M. Sheraz, S. Kim, *J. Korean Phys. Soc.* **2022**, *81*, 230–240.

[50] A. A. Petrov, E. A. Goodilin, A. B. Tarasov, V. A. Lazarenko, P. V. Dorovatovskii, V. N. Khrustalev, *Acta Crystallogr. E: Crystallogr. Commun.* **2017**, *73*, 569–572.

[51] J. Ibaceta-Jana, R. Muydinov, P. Rosado, H. Mirhosseini, M. Chugh, O. Nazarenko, D. N. Dirin, D. Heinrich, M. R. Wagner, T. D. Kühne, *Phys. Chem. Chem. Phys.* **2020**, *22*, 5604–5614.